ACTIVE FLOW CONTROL OF AN AIRCRAFT IN FULL STALL

***O. Lehmkuhl*[1], *I. Rodriguez*[2], *A. Lozano*[3]**

[1] ***Barcelona Supercomputing Centre, Barcelona, Spain***
[2] ***Universitat Politecnica de Catalunya, Barcelona, Spain***
[3] ***Dept of Aeronautics and Astronautics, MIT, Cambridge, USA***

oriol.lehmkuhl@bsc.es

Abstract

The aerodynamic performance of active flow control on wings using synthetic jets with zero net-mass flow is investigated. The study is conducted via wall-modeled large-eddy simulations using a finite-element-based solver. The performance of synthetic jets is evaluated for the high-lift configuration of the JAXA Standard Model at realistic Reynolds numbers for landing $Re_c = 1.96 \times 10^6$. The results show that, at high angles of attack, the control successfully eliminates the laminar/turbulent recirculations located downstream the actuator, which increases the aerodynamic performance. Our efforts illustrate the technology-readiness of large-eddy simulation in the design of control strategies for real-world external aerodynamic applications.

1 Introduction

The aerodynamic performance of an aircraft wing is significantly affected by the interaction of the flow with the nacelle and brackets, as well as by boundary-layer flow separation, specially at the high angles of attack (AoA) typically encountered during take-off and landing operations. At high angles of attack, the loss of momentum across the boundary layer leads to the flow separation and eventually the wing stall. In such situations, adding momentum to the flow might prevent the flow detachment, thus increasing the aerodynamic performance of the wing. The control of the boundary layer over wings has been the subject of many investigations in the past decades, studying different flow control techniques such as vortex generators, plasma actuators, synthetic jets, etc. Comprehensive reviews regarding these techniques can be found in [9, 6, 11]).

Several studies exploring the capabilities of AFC actuators in high-lift devices (i.e. suction and blowing, sweeping jets, fluidic oscillators, plasma actuators, synthetic jets) have been conducted. A brief review on the state of the art of active flow control techniques for civil aircrafts can be found Batikh et al. [4]. Radespiel et al. [26] reviewed different techniques for AFC using constant blowing showing that tangential blowing can be promising at increasing the lift at high angles of attack. Recent results published in the literature have shown that AFC can be beneficial for increasing the side force of an aircraft tail [31, 3] or that the use of microjets is interesting when it comes to drag reduction [16, 1].

The present work is focused on the application of synthetic jets with zero net mass flux as a promising technique for AFC of wings.Indeed, synthetic jets have been shown to succeed at reducing the fuel burnt during the operations of take-off and landing [12]. In the context of synthetic jets for AFC, there have been significant advances in the past years in airfoils (see, for instance, [22, 2, 10]). However, whether they can be implement on a full aircraft is still subject of investigation. Nonetheless, recent studies point out at their successful use to control separation in wings during short-duration operations (see for instance [13, 30, 5]).

In the present work, the use of synthetic jets for AFC of the wing boundary layer of a full aircraft in stall is explored by means of wall-modeled large-eddy simulations (WMLES). Slotted synthetic jets are located at both the main and slat of the JAXA Standard Model (JSM). This geometry was the subject of study in the recent 3rd AIAA CFD High Lift Prediction Workshop [29], where RANS-based methodologies, challenged to predict the onset of stall and maximum lift, had difficulties to predict the lift coefficient at high angles of attack AoA. A landing configuration with the high-lift devices (slat and flap) deployed in the absence of nacelle/pylon is considered at $Re_c = U_0 C/\nu = 1.93 \times 10^6$ and Mach number $M_0 = 0.15$. Here, the Reynolds number is defined in terms of the free stream velocity U_0 and the wing mean chord C. Ten different actuations strategies are explored to assess the impact of the different control parameters in stall conditions.

2 Mathematical formulation

In the present work, wall-modeled large-eddy simulations of the flow are performed. The incompressible spatially filtered Navier-Stokes equations read,

$$\frac{\partial \overline{u}_i}{\partial x_i} = 0$$
$$\frac{\partial \overline{u}_i}{\partial t} + \frac{\partial}{\partial x_j}(\overline{u}_j \overline{u}_i) = -\frac{\partial \overline{P}}{\partial x_i} + \frac{1}{Re}\nabla^2 \overline{u}_i - \frac{\partial \tau_{ij}}{\partial x_j} \quad (1)$$

The variables are normalized using the reference length L and reference velocity U_0, which define the Reynolds number $Re = U_0 L/\nu$, where ν is the kinematic viscosity of the fluid. The filtered velocity is $\overline{u}_i$, $\overline{P} = \overline{p}/\rho$ is the modified pressure, and $\tau_{ij} = \overline{u_i u_j} - \overline{u}_i \overline{u}_j$ is the subgrid-scale stress (SGS) tensor. The SGS stresses tensor is modeled using an eddy viscosity approach with its deviatoric part parametrized as

$$\tau^d_{ij} = \tau_{ij} - \frac{1}{3}\delta_{ij}\tau_{kk} = -2\nu_{\text{sgs}}\overline{S}_{ij} \quad (2)$$

where δ_{ij} is the Kronecker delta and

$$\overline{S}_{ij} = \frac{1}{2}\left(\frac{\partial \overline{u}_i}{\partial x_j} + \frac{\partial \overline{u}_j}{\partial x_i}\right) \quad (3)$$

is the strain-rate tensor. The formulation is closed by using a proper SGS viscosity, ν_{sgs}. In the present study the Vreman [34] model is used.

The simulations are performed using the code Alya [33], which is a parallel multi-physics/multi-scale simulation code developed at the Barcelona Supercomputing Center to carry out high-performance computations efficiently. In this work, second-order spatial discretizations are used. The convective term is discretized using a Galerkin finite element (FEM) scheme proposed by Charnyi et al.[7]. This scheme preserves linear and angular momentum, and kinetic energy at the discrete level. In the formulation used, neither upwinding nor any equivalent momentum stabilization is employed. Pressure stabilization, by means of a fractional step scheme [8], is introduced to use equal-order elements. This approach is similar to those used for pressure-velocity coupling in unstructured, collocated finite-volume codes [15]. An explicit third-order Runge-Kutta method combined with an eigenvalue-based time-step estimator [32] is used for the temporal integration of the equations. The current approach is less dissipative than the traditional stabilized FEM approach as shown in Lehmkuhl et al. [18].

In order to deal with the grid-resolution requirements necessary to well resolve the small-scale flow motions in the near-wall region, a wall model is here used. In the model, the no-slip boundary condition at the wall is replaced by a wall-stress boundary condition. The wall-shear stress from the algebraic equilibrium wall model is imposed as the wall boundary condition, and the wall is assumed to be isothermal. A finite element extension [24] of the wall law of Reichardt [27] is used:

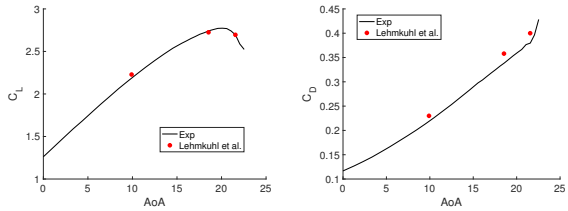

(a) (b)

Figure 1: Comparison of JSM results of the WMLES from Lehmkuhl et al. [19] with wind tunnel data from [35, 23]. (a) Lift coefficient, (b) Drag coefficient.

$$u^+ = \frac{1}{\kappa}\ln(1+\kappa y^+) + 7.8\left(1 - \mathrm{e}^{-y^+/11} - \frac{y^+}{11}\mathrm{e}^{-0.33y^+}\right) \quad (4)$$

where $y^+ = y_n\, u_\tau/\nu$, y_n being the wall normal distance and $u_\tau = \sqrt{\tau_w}$ the skin friction velocity and τ_w the wall normal shear-stress . The velocity is here normalized with the skin friction velocity as $u^+ = u_n/u_\tau$. The exchange location suggested by Kawai et al. [17] is here used.

3 Definition of the cases and computational domain

The JAXA Standard Model (JSM) in high-lift configuration, experimentally studied at JAXA [35, 23] is selected to investigate the different AFC strategies. The landing configuration with the high-lift devices, i.e. slat and flap, deployed is considered. The Reynolds number $Re_c = U_0\, C/\nu$ is $Re_c = 1.93 \times 10^6$ and the free-stream Mach number $M_0 = 0.17$. The nacelle/pylon components are not included in the simulations.

The performance of the WMLES in the JSM configuration was already assessed by Lehmkuhl et al. [19] at different angles of attack ($AoAs$) corresponding to the linear lift regime, maximum lift and stall conditions, i.e. at $AoA = 10,\ 18.58,$ and $21.57°$. In that study, a computational grid of about 65×10^6 collocation nodes was used. The results from the validation exercise, reproduced here for completeness in Figure 1, show that the lift coefficient is in good agreement with the experimental results; the drag coefficient is slightly over estimated compared to the experimental measurements. However, as discussed in [19], these differences might be due to the geometric differences between the computations and the experimental set-up.

Following the studies carried out in [19], present computations are performed in a domain of $x \equiv [-35.7,\ 142.8]$; $y \equiv [-71.43,\ 0]$ and $z \equiv$

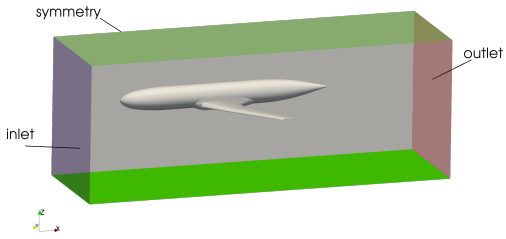

(a)

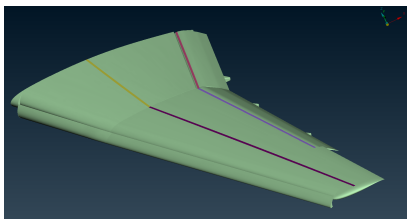

(b)

Figure 2: (a) Computational domain (not-to-scale) and (b) location of the slotted synthetic jets (main at $x/C = 0.5$ and flap at $x/C = 0.1$)

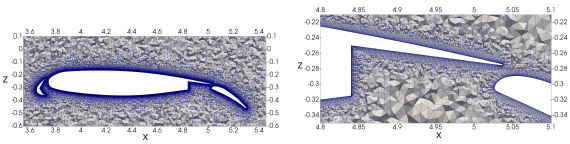

(a) (b)

Figure 3: Detail of the mesh used. (a) Mesh refinement at the wing at $y/C = 1$ (b) detail of refinement close to wall.

$[-71.43,\ 71.43]$ (see figure 2a). All sizes are normalized with the wing mean chord. The body is placed at $[x, y, z] \equiv [0, 0, 0]$. As we are interest in study the effect of the actuation on a high-lift configuration, in the present study the $AoA = 21.57°$ is considered. The actuation is imposed in both the main wing and the flaps, as shown in Figure 2b. The slotted actuators are located across the whole wing at $x/C = 0.5$ for the main, and at $x/C = 0.1$ for the flap wings; the width of the actuator is $h = 0.01C$.

The mesh here adopted is similar to that reported in Lehmkuhl et al. [19]. The mesh consist of 180 millions of finite elements, and is composed of anisotropic wedge/prism layers near the wall and tetrahedra elsewhere. Additionally, dedicated mesh density zones are designed to provide a proper mesh resolution in the wakes of the slant, flap, and main wings. A detail of the mesh used is shown in figure 3. The mesh is refined in the near-wall regions so that the number of grid cells across the local boundary layer thickness ranges from 5 to 10. Notice that with the wall-model the first node off the surface is located at about $y^+ \approx 30$.

A uniform plug flow as the inflow boundary condition, i.e. a uniform velocity profile $(u, v, w) = (U_0 \cos(AoA), 0,\ U_0 \sin(AoA))$, is set. At the outlet, the Navier–Stokes characteristic boundary condition for subsonic non-reflecting outflow and top planes is imposed [25]. Homogeneous Neumann boundary conditions are used in the symmetry plane. At the surface of the aircraft, the equilibrium model as described in the previous section is imposed. Actuation slots in the main wing and in the flaps are used. The main goal of the actuation is to control both the separation induced by the brackets connecting the slant and main wing, and the laminar separation bubbles in the flap region. At the outlet of the actuation line, the jet velocity v_i^{jet} (or $(u, v, w)_{jet}$ in x-, y- and z-direction) is defined as,

$$\begin{aligned}(u, v, w)_{jet} =& V_{max} \sin(2\pi f t) \cos(2\pi \tau_y y) \\ & (\cos\alpha, \sin\alpha, 1)(\sin\Phi, \sin\Phi, \cos\Phi)\end{aligned} \tag{5}$$

where f is the actuator frequency $F^+ = fC/U_0$, τ_y is the spanwise period of the signal (0 in 2D actuations and N_{jet}/L_y in 3D), V_{max} is obtained from $C_\mu = \frac{(\rho V_{max}^2)A_{act}}{(\rho U_0^2)A_{ref}}$, α is the angle with respect to the y-axis and Φ is the angle respect to the wing surface normal. The actuation can be two-dimensional (2D) across the whole slot area or three-dimensional (3D) where a slot period along the span is imposed. In the case of a 3D actuation, the outlet mimics a determined number of jets in the wing span (N_{jet}) adjusted to have a period $\tau_y = 0.1$. The period used here was proven to be successful at introducing momentum mixing to reduce the separation bubble formed on airfoils at low Reynolds numbers (see [28]).

The complete set of actuation cases is reported in Table 1. The set of cases comprises the variation of the actuation angle, the momentum coefficient and the frequency, as well as the effect of using a 2D actuation along the whole wing span.

4 Results

The results of the actuation for all cases are reported in figure 4 for the lift and aerodynamic efficiency in terms of the differences respect to the baseline case ($C_L = 2.685$, $C_D = 0.405$, $C_L/C_D = 6.63$). In general, except for cases 1-3, the lift is improved, the case 10 being the best situation, whereas in all cases aerodynamic efficiency is increased. Actually, the largest reduction in the drag is observed when actuation is only applied to the flap (case 2). However, the largest lift increase is observed when a combination of both actuation in the flap and main is applied (case 10).

The results of the actuation for all cases are reported in figure 4 for the lift and aerodynamic efficiency in terms of the differences respect to the baseline case ($C_L = 2.685$, $C_D = 0.405$, $C_L/C_D =$

Table 1: AFC considered parameters for the main wing and flap.

Case	$\Phi[deg]$	C_μ	F^+	$type$	$\Phi[deg]$	C_μ	F^+	$type$
		Main				Flap		
AFC1	0	0.015	1.52	3D	0	0.015	1.52	3D
AFC2	-	-	-	-	0	0.015	1.52	3D
AFC3	0	0.0075	1.52	3D	0	0.0015	1.52	3D
AFC4	-	-	-	-	0	0.0015	1.52	3D
AFC5	60	0.0075	1.52	2D	0	0.0015	1.52	3D
AFC6	60	0.015	1.52	2D	0	0.0015	1.52	3D
AFC7	60	0.0075	1.52	3D	0	0.0015	1.52	3D
AFC8	45	0.015	1.52	2D	0	0.0015	1.52	3D
AFC9	45	0.015	15.2	2D	0	0.0015	15.2	3D
AFC10	45	0.015/0.023	1.52	3D	0	0.0015	1.52	3D

6.63). In general, except for cases 1-3, the lift is improved the case 10 being the best situation, whereas in all cases aerodynamic efficiency is increased. Actually, the largest reduction in the drag is observed when actuation is only applied to the flap (case 2). However, the largest lift increase is observed when a combination of both actuation in the flap and main is applied (case 10).

To understand the effect of the actuation on the main wing, we inspect the flow patterns in the presence and absence of actuation. Figure 5 shows the mean streamlines for the un-actuated base flow and for cases AFC3, AFC6, and AFC8. The visualizations suggest that the main losses in the lift force are due to the formation of large separated zones. In the uncontrolled case, a large recirculation region occurs behind the flap, which lifts up the boundary layer in the rear end of the main wing right after the flow changes direction as induced by the flap deployment. For actuated cases with $\Phi = 0°$ (AFC1 and AFC3), the turbulent boundary layer is vertically displaced, which decreases the lift coefficient. When the actuation in the main wing is suppressed, the variations in the lift is very small, and the jet located at the flap can barely act on the recirculation zone. The present results suggest that $\Phi = 0^o$ is not a viable option to improve the lift forces, and the most efficient actuations are in the tangential direction with angles between $\Phi = 45^o$ and $\Phi = 60^o$. For $\Phi = 45°$, the jet is injected directly into the main boundary layer, enhancing mixing and preventing separation. The actuation strategies which approximates the best the ideal linear behavior of C_L are AFC8 and AFC10, with a slight improvement for case AFC10. In both cases, the large recirculation zone behind the flap is almost suppressed and the streamlines evolve parallel to each other behind the flap (see figure 5 bottom right and figure 6). Therefore, the actuator with spanwise-varying C_μ along the wing is effective in compensating for the geometrical changes in the wing.

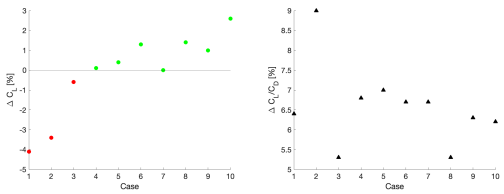

Figure 4: JSM high-lift at $Re_c = 1.93 \times 10^6$ and $AoA = 21.57^o$. AFC results. (left) Percentage of lift variation respect the baseline configuration. (rifgt) Percentage of variation of the aerodynamic efficiency

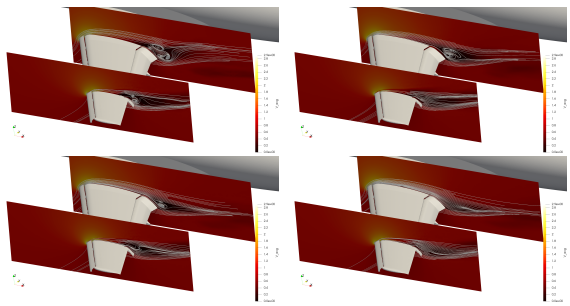

Figure 5: JSM high-lift at $Re_c = 1.93 \times 10^6$ and $AoA = 21.57^o$. 2D streamlines at different span-wise locations: baseline case vs different actuator jet angles. Top left) baseline; top right) AFC3($\Phi = 0^o$); bottom left) AFC6($\Phi = 60^o$); and bottom right) AFC8($\Phi = 45^o$).

5 Conclusions

Since the early days of aviation, many efforts have been devoted to the design of devices capable of providing the required lift, while reducing the associated drag of the device, such as slotted flaps or other high-lift mechanisms. Among the various approaches, active flow control via synthetic jets has emerged as a versatile technology for a broad range of applications at moderate and high Reynolds numbers. However, the use of CFD in the design of active flow control strategies for real-world applications has been hampered by

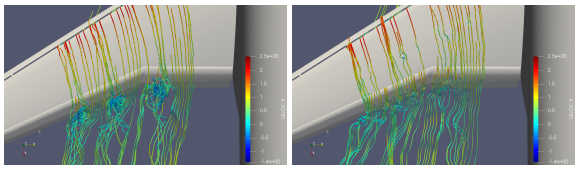

Figure 6: JSM high-lift at $Re_c = 1.93 \times 10^6$ and $AoA = 21.57^o$. Streamlines colored by non-dimensional streamwise velocity at the JSM high-lift wing: left) baseline configuration; right) AFC10.

the prohibitive computational cost associated with the computation of all the scales of the motions typically encountered in turbulent flows.

In the present work, we have investigated the impact of AFC on the aerodynamic performance of actuated high-lift wings. To make the problem tractable, the methodology employed has been wall-resolved and wall-modeled LES. A systematic study of the effect of synthetic jets is addressed by performing a campaign of WMLESs varying the jet inclination angle relative to the solid boundary, the value of the momentum coefficient, actuating jet frequency, and the number of actuation lines (flaps or wing+flaps). The comprehensive matrix of cases provides rich information about the impact of the AFC on the flow. The most effective control in terms of aerodynamic performance (with 6.2% improvement) is achieved for jets with 45 degrees inclination angles, frequencies of $F^+ = 1.52$, and variable spanwise momentum coefficient along the wing. Interestingly, cases where the actuation is limited to the flaps reveal that the additional momentum injected into the boundary layer occurs too late downstream flow to efficiently remove the recirculation pattern.

Acknowledgments

This work is funded in part by the Coturb program of the European Research Council. O. L. acknowledges the financial support by the Ministerio de Economía y Competitividad, Secretaría de Estado de Investigación, Desarrollo e Innovación, Spain (ref. TRA2017-88508-R) and the European Union's Horizon 2020 research and innovation programme (INFRAEDI-02-2018, EXCELLERAT- The European Centre Of Excellence For Engineering Applications H2020.). We also acknowledge Red Española de Supercomputación and Barcelona Supercomputing Center for awarding us access to the MareNostrum IV machine based in Barcelona, Spain (FI-2018-3-0021, FI-2018-2-0015, FI-2018-1-0022, FI-2017-3-0024). A.L.-D. acknowledges the support of NASA Transformative Aeronautics Concepts Program (Grant No. NNX15AU93A) and the Office of Naval Research (Grant No. N000141712310).

References

[1] Aley, K.S., Guha, T.K, and Kumar, R.. Active Flow Control of a High-Lift Supercritical Airfoil with Microjet Actuators. *AIAA Journal*, pages 1–17, 2020.

[2] Amitay, A. and Glezer, G. Role of actuation frequency in controlled flow reattachment over a stalled airfoil. *AIAA Journal*, 40(2):209–216, 2002.

[3] Andino MY, Lin JC, Roman S, Graff EC, Gharib M, Edward A. Whalen, and Israel J. Wygnanski. Active Flow Control on Vertical Tail Models. *AIAA Journal*, 57(8):3322–3338, 2019.

[4] Batikh A, Baldas L, and Colin S. Application of Active Flow Control on Aircrafts - State of the Art. *International Workshop on Aircraft System Technologies*, pages 1–10, 2017.

[5] Bauer M, Lohse J, Haucke F, and Nitsche W. High-Lift Performance Investigation of a Two-Element Configuration with a Two-Stage Actuator System. *AIAA Journal*, 52(6):1307–1313, 2014.

[6] Cattafesta LN and Sheplak M. Actuators for Active Flow Control. *Annual Review of Fluid Mechanics*, 43(1):247–272, 2011.

[7] Charnyi S, Heister T, Olshanskii MA, and Rebholz LG. On conservation laws of Navier-Stokes Galerkin discretizations . *Journal of Computational Physics*, 337:289 – 308, 2017.

[8] Codina R. Pressure stability in fractional step finite element methods for incompressible flows. *J. Comput. Phys.*, 170:112–140, 2001.

[9] Corke TC, Enloe CL, and Wilkinson SP. Dielectric Barrier Discharge Plasma Actuators for Flow Control. *Annual Review of Fluid Mechanics*, 42(1):505–529, 2010.

[10] Gilarranz J. L. , Traub L. W., and Rediniotis O. K.. A New Class of Synthetic Jet Actuators—Part I: Design, Fabrication and Bench Top Characterization. *Journal of Fluids Engineering*, 127(2):367, 2005.

[11] Glezer A. Some aspects of aerodynamic flow control using synthetic-jet actuation. *Philosophical Transactions of the Royal Society A: Mathematical, Physical and Engineering Sciences*, 369:1476–1494, 2011.

[12] Hartwich PM, Shmilovich A, Lacy DS, Dickey ED, Anthony J. Scalafani, P. Sundaram, and Yoram Yadlin. Refined AFC-Enabled High-Lift System Integration Study. Technical Report CR-2016-219170, 2016.

[13] Jabbal M. , LiddleS. C. , and Crowther W. J. Active flow control systems architectures for civil transport aircraft. *Journal of Aircraft*, 47(6):1966–1981, 2010.

[14] Jansen KE, Rasquin M, Farnsworth JA , Rathay N, Monastero MC, and Amitay M. Interaction of a Synthetic Jet with Separated Flow over a Vertical Tail. *AIAA Journal*, 56(7):2653–2668, 2018.

[15] L. Jofre, O. Lehmkuhl, J. Ventosa, F.X. Trias, and A. Oliva. Conservation properties of unstructured finite-volume mesh schemes for the Navier-Stokes equations. *Numerical Heat Transfer, Part B: Fundamentals*, 54(1):53–79, 2014.

[16] Kara K, Kim D, and Morris PJ. Flow-separation control using sweeping jet actuator. *AIAA Journal*, 56(11):4604–4613, 2018.

[17] S. Kawai and J. Larsson. Wall-modeling in large eddy simulation: Length scales, grid resolution, and accuracy. *Phys. Fluids*, 24(015105), 2012.

[18] O. Lehmkuhl, G. Houzeaux, H. Owen, G. Chrysokentis, and I. Rodriguez. A low-dissipation finite element scheme for scale resolving simulations of turbulent flows. *Journal of Computational Physics*, 390:51 – 65, 2019.

[19] O Lehmkuhl, G Park, ST Bose, and P Moin. Large-eddy simulation of practical aeronautical flows at stall conditions. In *Center for Turbulence Research-Proceedings of the Summer Program*, pages 87–96, 2018.

[20] Lin JC, Melton, Hannon J, Andino M, Koklu M, Paschal K, and Vatsa VN. Wind tunnel testing of active flow control on the high lift common research model. In *AIAA Aviation 2019 Forum*.

[21] Lin JC, Pack Melton, Viken S, Andino MY, Koklu M, Hannon J, and Vatsa VN. High Lift Common Research Model for Wind Tunnel Testing: An Active Flow Control Perspective. In *55th AIAA Aerospace Sciences Meeting*, 2017.

[22] D C Mccormick. Boundary Layer Separation control with Directed Synthetic Jets. In *38th Aerospace Sciences Meeting & Exhibit*, number AIAA 2000-0519, 2000.

[23] Mitsuhiro Murayama, Yuzuru Yokokawa, Kazuomi Yamamoto, and Yoshine Ueda. Evaluation of computations and transition prediction method for aircraft high-lift configuration. *Journal of Aircraft*, 46(5):1487–1499, 2009.

[24] Herbert Owen, Georgios Chrysokentis, Matias Avila, Daniel Mira, Guillaume Houzeaux, Ricard Borrell, Juan Carlos Cajas, and Oriol Lehmkuhl. Wall-modeled large-eddy simulation in a finite element framework. *International Journal for Numerical Methods in Fluids*, 2019.

[25] T.J Poinsot and S.K Lelef. Boundary conditions for direct simulations of compressible viscous flows. *Journal of Computational Physics*, 101(1):104 – 129, 1992.

[26] R. Radespiel, M. Burnazzi, M. Casper, and P. Scholz. Active flow control for high lift with steady blowing. *Aeronautical Journal*, 120(1223):171–200, 2016.

[27] H. Reichardt. Vollständige darstellung der turbulenten geschwindigkeits- verteilung in glatten leitungen. *ZAMM-Z. Angew. Math. Me.*, 31:208–219, 1951.

[28] I. Rodriguez, O. Lehmkuhl, and R. Borrell. Effect of the Actuation on the Boundary Layer of an Airfoil at Reynolds Number Re=60000. *Flow, Turbulence and Combustion*, 105:313–319, 2020.

[29] Christopher L Rumsey, Jeffrey P Slotnick, and Anthony J Sclafani. Overview and summary of the Third AIAA High Lift Prediction Workshop. *AIAA P.*, 2018. 2018-1258. Also, https://hiliftpw.larc.nasa.gov/.

[30] A. Shmilovich and Y. Yadlin. Active flow control for practical high-lift systems. *Journal of Aircraft*, pages 1354–1364, 2009.

[31] Arvin Shmilovich, Yoram Yadlin, and Edward A. Whalen. Active flow control computations: From a single actuator to a complete airplane. *AIAA Journal*, 56(12):4730–4740, 2018.

[32] F. X. Trias and O. Lehmkuhl. A self-adaptive strategy for the time integration of Navier-Stokes equations. *Numerical Heat Transfer. Part B*, 60(2):116–134, 2011.

[33] A. M. Vazquez, G. Houzeaux, S. Koric, A. Artigues, J. Aguado-Sierra, R. Aris, D. Mira, H. Calmet, F. Cucchietti, H. Owen, E. Casoni, A. Taha, E. D. Burness, J. M. Cela, and M. Valero. Alya: Multiphysics engineering simulation towards exascale. *J. Comput. Sci.*, 14:15–27, 2016.

[34] A. W. Vreman. An eddy-viscosity subgrid-scale model for turbulent shear flow: Algebraic theory and applications. *Physics of Fluids*, 16(10):3670–3681, 2004.

[35] Yuzuru Yokokawa, Mitsuhiro Murayama, Masahiro Kanazaki, Katsuichi Murota, Takeshi Ito, and Kazuomi Yamamoto. *Investigation and Improvement of High-Lift Aerodynamic Performances in Lowspeed Wind Tunnel Testing*.